Experimental analysis and simulation of low-velocity impact damage of composite laminates

Falcó, O.; Lopes, C. S.; Sommer, D. E.; Thomson, D.; Ávila, R. L.; Tijs, B. H.A.H.

DOI
10.1016/j.compstruct.2022.115278

Publication date
2022

Document Version
Final published version

Published in
Composite Structures

Composite Structures 287 (2022) 115278

Contents lists available at ScienceDirect

Composite Structures

journal homepage: www.elsevier.com/locate/compstruct

Experimental analysis and simulation of low-velocity impact damage of composite laminates☆

O. Falcó [a,b,*], C.S. Lopes [b,c], D.E. Sommer [a], D. Thomson [a], R.L. Ávila [d], B.H.A.H. Tijs [e,f]

[a] Department of Engineering Science, University of Oxford, Oxford, United Kingdom
[b] IMDEA Materials — Madrid Institute for Advanced Studies of Materials, Tecnogetafe, Madrid, Spain
[c] Luxembourg Institute of Science and Technology, Esch-sur-Alzette, Luxembourg
[d] Autonomous University of Coahuila, Saltillo, Mexico
[e] GKN Aerospace: Fokker, Papendrecht, The Netherlands
[f] Delft University of Technology, Faculty of Aerospace Engineering, Delft, The Netherlands

ARTICLE INFO

Keywords:
Carbon fibre reinforced polymer
Impact behaviour
Finite Element Analysis (FEA)
Computational modelling

ABSTRACT

The capability to accurately analyse the response of multi-directional composite laminates during impact events is of high importance for the design of lightweight aircraft structures. In this work, both experimental and numerical analyses are performed covering a large design-space of laminates for all aspects from on-set of damage and barely visible impact damage up to clearly visible impact damage and full penetration of the laminates. The impact tests are simulated using a sophisticated three-dimensional continuum damage model, combined with an automated meso-scale model generation algorithm for ply-by-ply, material/fibre-aligned meshing of laminated composite coupons. To assess the accuracy of the predictions, an extensive validation test program of several configurations and impact energies has been performed, thus demonstrating that the simulations are capable of accurately predicting the damage and failure mechanisms under low-velocity impact loading. Not only the evolution of impact loads and energy dissipated are numerically analysed, but the competition of the dominant failure mechanisms from low impact energy and full penetration cases are also macroscopically replicated.

1. Introduction

Damage resistance of composite materials under impact events and their residual strength is a key factor in the design of aircraft structures. However, it is difficult to optimize the design of these structures due to the vast amount of design possibilities and it requires extensive and costly experimental trial-and-error testing campaigns to meet certification requirements. The impact event can happen during manufacturing, servicing or maintenance operations, such as tool dropping. While barely visible small indentations are produced on the surface by low energy impacts, internally, structures are degraded in a variety of hidden failure mechanisms such as fibre breakage, matrix cracking, kink-banding and delamination. As it is difficult to detect these damages during inspections, this means that aircraft structures have to be designed to account for Barely Visible Impact Damage (BVID). The terminology is introduced to describe structural damage or defects in relation to inspection procedures used in the aerospace industry. Low-Velocity Impact (LVI) and Compression After Impact (CAI) tests are commonly used for the evaluation of damage resistance and residual strength of composite materials to develop design data. However, due to the massive number of design variables, material properties and the complexity for the analysis of failure mechanisms, reliable design tools and novel damage modelling approaches have received considerable interest of the transportation sector.

Simplified and high-fidelity computational models have been developed by several authors to investigate LVI for composite laminates [1–3]. Bogenfeld et al. [4] present a detailed review and benchmark study for impact simulation modelling techniques, concluding that the best meso-scale modelling approach for the analysis of impact damage, should include the combination of both, cohesive surfaces and finite solid elements. Examples of LVI and CAI simulations using this approach by applying stacked layer models formulated in the context of continuum damage mechanics (CDM) can be found in [5–8]. These works primarily employ detailed meso-scale (ply-by-ply meshing) simulations that combine cohesive zone modelling (CZM) to predict the

☆ This paper is dedicated to the memory of our dear colleague C.S. Lopes (Deceased November 2020).

* Correspondence to: Impact Engineering, Laboratory (IEL), University of Oxford, Department of Engineering Science, Begbroke Science Park, Begbroke Hill, Woodstock Road, Oxfordshire, OX5 1PF, United Kingdom.
E-mail addresses: olben.falcosalcines@eng.ox.ac.uk (O. Falcó), bas.tijs@fokker.com (B.H.A.H. Tijs).

https://doi.org/10.1016/j.compstruct.2022.115278
Received 29 October 2021; Received in revised form 18 January 2022; Accepted 19 January 2022
Available online 8 February 2022

interlaminar failure and CDM for intra-ply damage. To achieve better level of detail in terms of damage predictions, high-fidelity models are recommended, although massive computation and modelling efforts will be required. Both Bouvet et al. and Shi et al. [9,10], proposed a model to predict the permanent indentation caused by LVI, validated on a single reference layup at a given impact energy. Preventing closure of matrix cracks was used to simulate "impact debris". An extension of Bouvet's work, was performed by Hongkarnjanakul et al. [11], changing impact conditions for validation of the initial model by using different stacking sequences, for a single impact energy value of 25 J. In addition, Rivallant et al. [12] used the same modelling approach, to perform numerical simulations of impact damage, permanent indentation and CAI for different impact energy values for a single laminate configuration. Delaminations, matrix cracking and their interaction were simulated using interface elements based on fracture mechanics and intralaminar failure criteria, respectively. In all these previous works, the overall goal was to capture the macroscopic behaviour and the interaction of failure mechanisms described by delaminations, fibre failure, and matrix damage, as well as a physically sound kinematic response.

As a general overview, despite the evolution of modelling techniques for the analysis of composite materials under transverse loading such as impact, the capability to efficiently predict both interlaminar and intralaminar damage mechanisms, as well as permanent indentation, still remains a challenging task. Although several previous works showed good predictions in comparison with experimental results, relatively few laminate configurations were analysed in each study. In most cases, very simple stacking sequences, such as quasi-isotropic or cross-ply layups, were evaluated for few impact energy values or cases without full penetration [13,14]. In addition, most studies focused on the prediction of interlaminar damage, with less importance given to the physical prediction of intralaminar damage mechanisms [15–19]. Furthermore, other numerical modelling approaches required calibration of the input parameters through a numerical tuning process e.g. by considering fracture energy balance criteria [20,21].

In terms of intralaminar damage in particular, a remarkable improvement in the modelling technique for the predictions of the material cracks can be achieved by including aligned-mesh structuring. Sun et al. [22] implemented a modelling approach using interface elements with a CZM approach to model the local response of delamination, matrix cracks and their interaction for a static indentation virtual test. Further analysis compared high-fidelity 3D solid finite element with a coupled solid/shell modelling technique. This approach was suitable for capturing the global damage behaviour in larger scale structures under low-velocity impact events [23]. It was concluded that level of correlation in terms of damage predictions increases with the number of potential intralaminar crack paths inserted in the model and aligned with the material orientations. A similar modelling approach using interface elements with CZM formulations was used by Bouvet et al. [9,24], implementing a Discrete Ply Modelling (DPM) combined with a user-defined 'VUMAT' subroutine using aligned-meshes, where positions of nodes are uniformly stacked in row and column for all oriented plies. Zero-thickness 3D cohesive elements were used to impose the region of matrix cracking for the prediction of both intra and interlaminar damage modes. By using this 'ply-splitting' technique, cracks were captured as real singularities in the ply. A similar structured-aligned mesh discretization with coincident node locations through thickness, was used by Lopes et al. [25], but in the context of a CDM approach, as a less expensive alternative to the discrete approach, combined with CZM formulations for the interlaminar damage prediction. However, using this mesh procedure, only stacking layups with conventional material orientation angles can be addressed and the plies with ±45° were meshed with 'diamond' shaped elements. In order to overcome this limitation for modelling complex stacking sequences, Trellu et al. [26] developed a user element for delamination calculation in non-conforming meshes, allowing the definition of an interface corresponding to the overlapping zone between the two volume elements. Another solution to tackle this problem is by using a 'surface-based cohesive' contact formulation, available as standard feature in most commercial FEA software packages.

The CDM modelling approach based on aligned-mesh structuring and crack-band erosion is suited to capture the crack paths and complex interactions between competing damage modes. However, model size in CDM analysis can be increased due to the limited element characteristic length and requirement of having to place the refined mesh over all potentially damageable regions for the homogenization of cracks. Optimization of these damage zones is a critical factor to avoid compromising the efficiency of the analysis. Recent advances in the area of computational damage mechanics and meso-scale modelling of multidirectional fibre-reinforced laminated composites have been deployed in a virtual testing framework to simulate the mechanical performance of un-notched and open-hole coupons under tension and compression, for both conventional and dispersed stacking sequence laminates [27,28]. Despite the computational cost of these models, they can produce many insights into the mechanical behaviour and aid in the development of the experimental testing and design allowables. While previous efforts were applied primarily to in-plane loading, in this work, the virtual testing framework is extended to out-of-plane loading cases. The intention is to demonstrate that the implemented methodology is robust enough to perform reliable virtual testing of multi-directional laminates for general loading conditions. More application and improvement by the authors for the prediction of matrix dominated failure modes and ply splitting using this framework with aligned mesh can be found respectively in [29,30].

The originality of this work is focused not only on validating the proposed modelling approach by correlating the numerical simulations across a sufficiently wide range of cases with different layup configurations, but also for several impact energy values including cases with full penetration. The implemented framework can capture the complexity of the physical phenomena, which includes dynamic structural behaviour and loading, contact interactions, friction, damage and failure. In addition, the underlying idea behind the present research, is that reliable constitutive modelling alone may not be enough to guarantee accurate FE simulation of both damage and failure in composite materials. It needs to be associated with a good kinematic description of the laminate failure modes and a proper modelling discretization using fibre-aligned meshes. By using this combination, competitions and interaction of different damage modes and failure patterns can be realistically predicted. The CDM proposed here avoids the use of CZM at all element interfaces used by the discrete methods mentioned before, which penalize the numerical efficiency. This study demonstrates that not only qualitatively similar results can be achieved, using CDM, but also a high detailed reconstruction of the damage mechanisms, by using mesh-alignment and element erosion techniques. Some previous works have applied extended finite element approaches with high complexity [31] or advanced methods like phase field modelling [32], which require more development and maturity for application on impact loading scenarios in laminated composites.

In this paper, the modelling strategy has been improved and combined with different physically-based damage models to predict the material behaviour under LVI. The virtual laboratory is embedded in a commercially-available explicit FE solver tool (ABAQUS/Explicit [33]), including the following as main characteristics. A three-dimensional CDM for unidirectional FRP plies, implemented through a user-defined 'VUMAT' subroutine with explicit integration scheme, is used to model intralaminar failure. The improvements of this formulation include among others: first, an extension to three-dimensional loading scenarios of the initial plane stress formulation proposed by Maimí et al. [34]. Second, a more accurate physically-based failure criteria, which takes into account the three-dimensional stress states and *in-situ* effects for the prediction of the onset of matrix cracking and fibre fracture [35].

These aspects are considered to be important for the analysis because significant out-of-plane loading is presented due to the bending behaviour during the impact. Third, the modification of Bažant's crack band model [36], to ensure a mesh independent solution by using two independent element characteristic lengths. A surface-based cohesive-frictional modelling algorithm (native of ABAQUS/Explicit) to model ply interfaces is used. These characteristics are relevant to predict permanent indentation which is taken into account and simulated by using nonlinear shear formulation of the intra-laminar damage model and by cohesive surface interaction combined with static friction of opposing crack planes preventing the delamination from closing. An automated meso-modelling generator for multi-directional laminated coupons with controlled mesh size, ply-by-ply mesh-alignment and directional biasing to predict damage localization along physically-sound crack paths permits rapid model creation. Rotated, perfectly rectangular elements have been used instead of diamond shapes. In addition, the initial mesh generator was improved to allow different mesh discretization of components or damageable zones, which can be extended until coupon edges or just in a central area.

Finally, the highly detailed and extensive experimental campaign is used to validate the numerical simulations by comparing the force–displacement curves, energy absorption, impactor velocities and fracture morphology. An analysis of the predicted delamination areas is presented for all laminates impacted at BVID energy threshold values and the computational cost of the simulation campaign is also discussed. Overall, good agreement between the simulations and experiments is observed. Several cases are reported demonstrating the strengths and weaknesses of the implemented approach.

2. Low-velocity impact testing and experimental results

The experimental campaign follows the set-ups provided by a standard test method from Airbus, AITM1-0010 [37], for measuring the damage resistance of a fibre-reinforced polymer matrix composite laminates when subjected to a drop-weight impact event. In this test, the impact load and the evolution of the absorbed energies were monitored using a commercially available Instron Ceast 9350 (Fractovis Plus, Italy) instrumented drop-weight tower, with a 12.7 mm diameter hemispherical impactor (D) and an automatic anti-rebound impactor system. The damage induced by a low velocity impact event is evaluated by measuring size of the indentation and extent of the interlaminar delaminations. Equivalent guideline for a drop-weight impact test provided by the aeronautical industry can be found in ASTM D7136/D7136M-05 [38] and Boeing 7260 [39]. One difference between the AITM1-0010 and ASTM D7136/D7136M-05 or Boeing 7260 is the location of the clamps. In the former case, the clamps are located inside the support cut-out region.

The specimens with 150 × 100 mm in-plane dimensions are placed over a flat support fixture base with a 125 × 75 mm rectangular cut-out which allows the impactor to contact through the specimen without interferences and centrally positioned by using guiding pins. The impact tester is equipped with a load cell of 22 kN attached to the impactor, an automatic pneumatic rebound brake system, and an edge support in accordance to AITM1-0010 [37]. Four clamps were used to restrain the specimen during impact with a minimum holding capacity of 1100 N [38] (see Fig. 1).

2.1. Experimental test matrix

The experimental test matrix includes five different laminate configurations with the following percentage ratios of plies in the 0°, ±45°, and 90° directions: 30/60/10 (361), 33/50/17 (351), 25/50/25 (252), 10/80/10 (181T), where (T) is to account for thick laminates and 12.5/75/12.5 (181). The corresponding stacking sequences are presented in Table 1. The laminates are all balanced and symmetric, and contain both dispersed and lumped plies. The laminates studied here are all relatively soft with the highest percentage of 0° plies being 33%. The different laminates will be referred to by the aforementioned ply percentage ratios for the remainder of the paper. Laminates were manufactured at GKN Aerospace: Fokker facilities in The Netherlands, and cured in an autoclave following the cycle specified by the supplier. All panels were inspected with C-scans before testing to verify the consolidation quality. Measurements of the panel thickness indicate that the panels were reasonably uniform and within tolerance according to the test standards. After curing the laminates, the specimens were cut using a 2.5 mm thick diamond blade at IMDEA Materials Institute, Spain.

2.2. Experimental evaluation of the barely visible impact damage energy threshold

Drop-weight impact tests are performed to the study the damage resistance to low-velocity impact at several impact energies in order to determine the required BVID impact energy for each laminate. After impact testing, C-scans are performed to determine to size and location of the delaminations and the indentation depth is measured. The BVID energy threshold is defined by the impact energy value that results in 1 mm (E_{1mm}) of permanent dent [40]. The specimens were subjected to drop-weight impact, in a range of energy values between 10 J to 70 J. Since the repeatability of the drop-weight impact test is acceptable, only one sample for impact energy value was used. Whereas two specimens of each configuration where impacted for both 30 J and impact energy threshold. In order to determine the threshold of BVID, the permanent indentation d_{dent} was measured 30 min after the impact event using a depth gauge and equation ($d_{dent} = d_{max} - d_{mean}$) [37]. For all tested configurations, a record of indentation depth as a function of the impact energy and BVID energy threshold is shown in Fig. 2(a). In general, indentation depth was increasing with increasing impact energy until the full penetration of the laminate. Similar energy thresholds were found for the configurations with approximately similar thickness and percentage ratios of plies with 0°, whereas the maximum energy value of 60 J was reached for the thicker configuration 361. An example of permanent indentation on the impacted face and the associated matrix cracks on the non-impacted face is illustrated on Fig. 2(b) for a configuration 252 impacted at 33 J.

2.3. Impact load, delamination threshold and absorbed energy evolution analysis

A comparison of the corresponding histories of the impact loads as a function of the impactor displacement for each laminate configuration impacted with an energy value of 30 J are shown in Fig. 3(a, b). The analysis of the impact load evolution determines the delamination threshold load F_d, the peak load F_p and the displacement evolution of the impactor. The maximum force recorded during the impact process is determined by the peak load F_p, whereas F_d is identified by the first significant drop in the impact load, and represents the initial load at which a significant change in the laminate stiffness is detected. In addition, this value is also associated with the development of a first significant delamination. After this point, the material behaviour is affected by the competition of several failure mechanisms. Fibre breakage and matrix cracking can be located at the impacted zone, whereas fibre–matrix interface debonding and large delamination due the bending forces can be found throughout the laminate. At this impact energy level, the maximum displacement with rebound was registered for the particular case of the configuration 181T, whereas for the configuration 181 full penetration was obtained by reducing considerably the bending stiffness of the structure.

The impact force history $F(t)$ is used to compute the velocity $V(t)$ and displacement history of the impactor $w_i(t)$ by integrating the force history once and twice respectively, declared as follows:

$$V(t) = V_0 + gt - \int_0^t \frac{F(t)}{M_i} dt \tag{1}$$

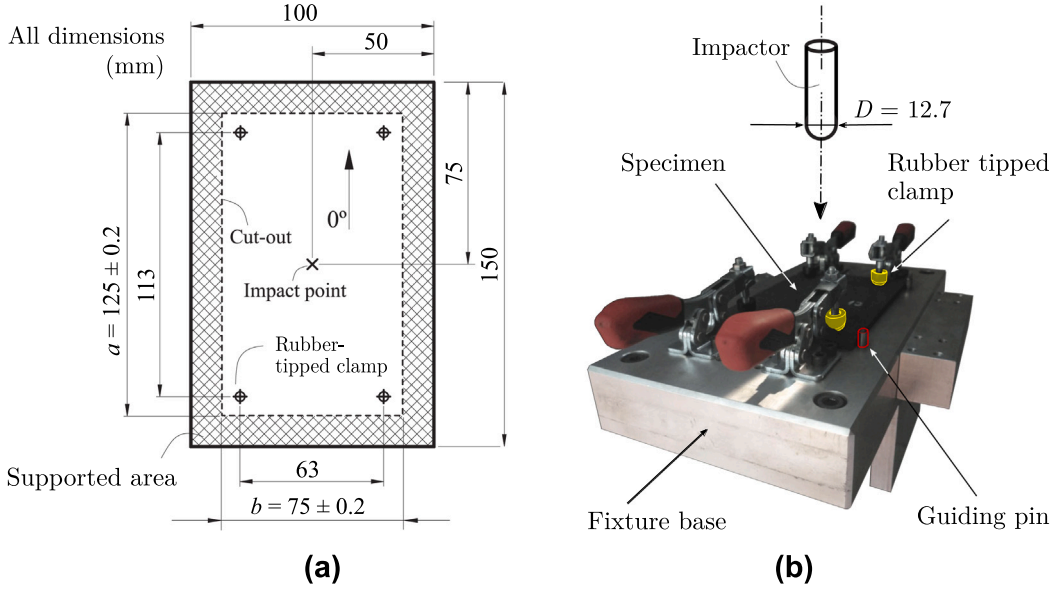

Fig. 1. (a) Specimen dimensions and detail of the support area and clamping points; (b) Impact support fixture system.

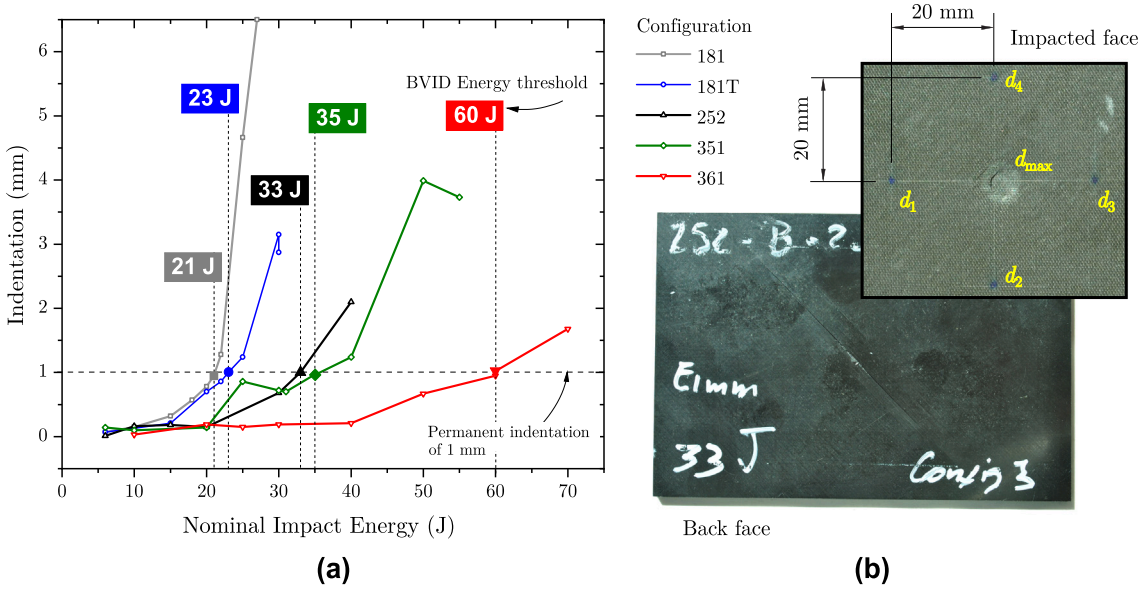

Fig. 2. (a) BVID threshold and experimentally-obtained relations between impact energy and indentations; (b) identification of permanent indentation for a configuration 252 impacted at 33 J [29].

Table 1
Test specimen layup definitions.

Laminate	t [mm]	Layup	0° plies	±45° plies	90° plies
181	2.944	[45/-45/0/45/45/-45/-45/90]s	12.5%	75%	12.5%
181T	3.680	[45/-45/0/45/-45/90/45/-45/45/-45]s	10%	80%	10%
252	4.416	[45/0/-45/90/45/0/-45/90/45/0/-45/90]s	25%	50%	25%
351	4.416	[45/0/-45/0/45/0/-45/90/45/90/-45/0]s	33%	50%	17%
361	6.256	[45/0/-45/0/-45/45/0/-45/90/45/45/90/-45/0/0/-45/45]s	30%	60%	10%

$$w_i(t) = V_0 t + \frac{gt^2}{2} - \int_0^t \left(\int_0^t \frac{F(t)}{M_i} dt \right) dt \tag{2}$$

where V_0 is the initial impactor velocity, (g) is the acceleration due to the gravity with value of $(9.81\ m/s^2)$ and (M_i) is the impactor mass [38].

A comparison of the elastic stiffness and the maximum impact force between all configurations impacted at 30 J is shown in Fig. 3(c). The first part of the results is the elastic regime of the impact process and the delamination threshold starts almost at the same time but with different values. The laminates with maximum and minimum elastic stiffness correspond with the thicker configuration 361 and thinner 181 respectively. Whereas very similar stiffness was found for laminates 351 and 252 with equivalent thickness and bending. For laminates 181 and 181T the impact time increases because the bending stiffness of the structure is reduced. With respect to the other configurations, 30

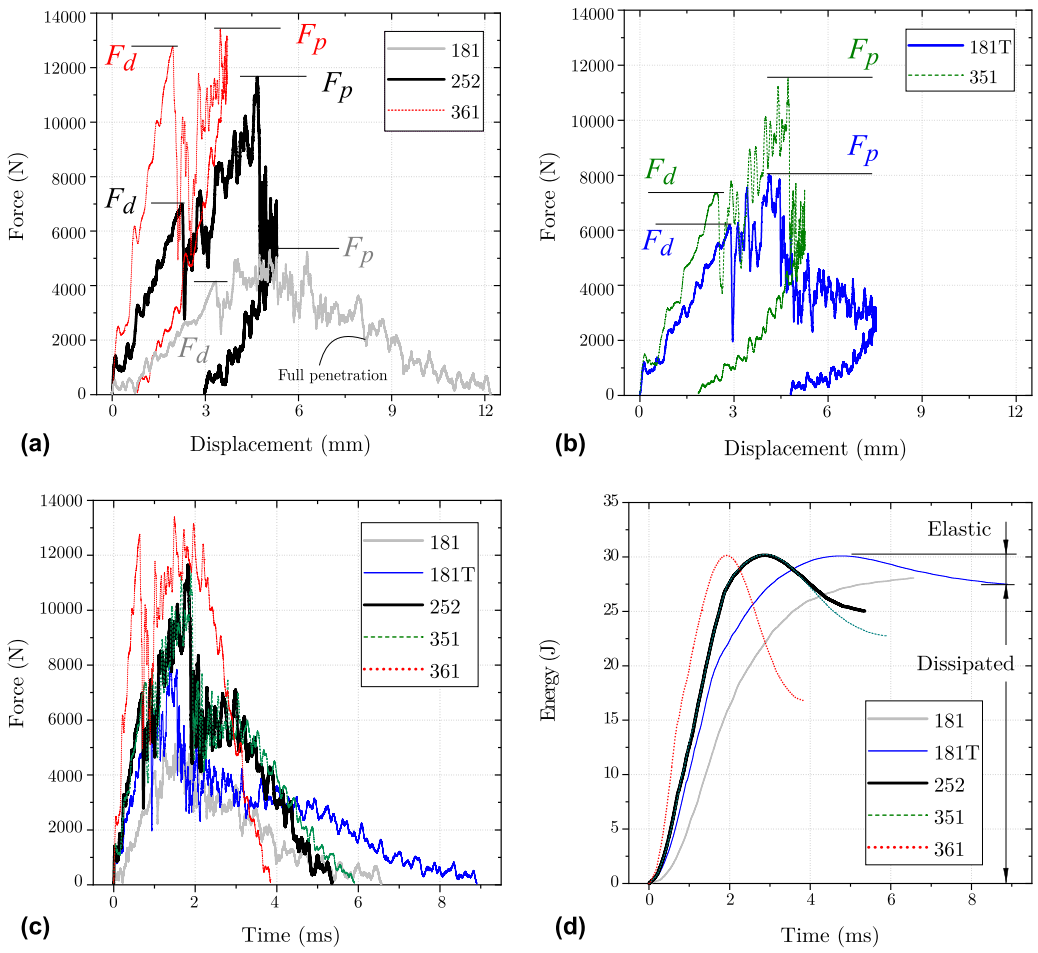

Fig. 3. (a, b) Impact load evolution in function of displacement with impact energy 30 J; (c, d) Comparison for both impact load evolution and evolution of the absorbed energies for all tested laminates impacted at 30 J respectively. The elastic energy and the dissipated energy are represented in the plot (d).

J corresponds to a laminate damage level below the BVID threshold. As expected, the minimum out-of-plane displacement was associated to the thicker configuration 361. In addition, this particular configuration presented the lowest difference between delamination threshold load F_d and peak load F_p in comparison with the others. This indicates that changes in the stiffness during the impact are more progressive and smooth for thicker laminates than for thinner laminates.

The absorbed energy evolution for each laminate for an impact energy of 30 J is shown in Fig. 3(d). This plot shows how the impactor's kinetic energy is transferred to the laminate. This energy is dissipated mainly by means of friction between the impactor and the laminate and between the competition of different failure mechanisms, which include indentation at the impact face, interlaminar delaminations, tensile matrix cracking and fibre breakage triggered by local stresses. For cases without full penetration of the impactor, part of the kinetic energy it temporarily accumulated as elastic strain energy and transferred back to the impactor. A portion of the accumulated energy is kept in the form of specimen vibrations and dissipated by damping. At this particular impact energy of 30 J, it is clearly illustrated how the major dissipated energy values correspond with laminates 181 and 181T. For the particular laminate 181 full penetration without impactor rebound took place, and the impact energy was completely dissipated. Laminates 252 and 351 showed equal bending stiffness although the absorbed energy for the laminate 252 was slightly greater. For the laminate with lowest dissipated energy, close to the 50% of the impacted energy was associated with the thicker configuration 361.

The energy absorbed by the specimen, $E_a(t)$, can be calculated using the following expression:

$$E_a(t) = \frac{M_i \left(V_0^2 - V(t)^2\right)}{2} + M_i g w_i(t) \tag{3}$$

A clear demonstration that the delamination threshold F_d is independent of the impact energy is shown in Fig. 4(a). In this figure, the impact load is plotted as a function of the projectile displacement for a single configuration, 181, impacted with five different impact energy values. In all cases, the delamination threshold was observed to be almost constant with a F_d value around 4000 N, even for the particular cases with full penetration impacted at 30 J. In addition, the projected delamination areas were not affected by increasing the impact energies beyond the BVID energy threshold. One explanation of this behaviour can be attributed to the fact that the energy is dissipated mainly due to crushing of the laminate. This is illustrated in Fig. 4(b) where the delamination due to back-splitting is removed for the higher impact energies.

2.4. C-scan after impact

After impact, ultrasonic C-scan inspections were performed to identify the projection of the delamination areas over the impacted specimen through thickness. In this work the delamination areas at ply level have been neglected and only the damage footprints were approximately measured and illustrated in Fig. 5. For impact energy values below the energy threshold BVID, a circular shape of the projected area was observed. Whereas for higher impact energy values, the areas

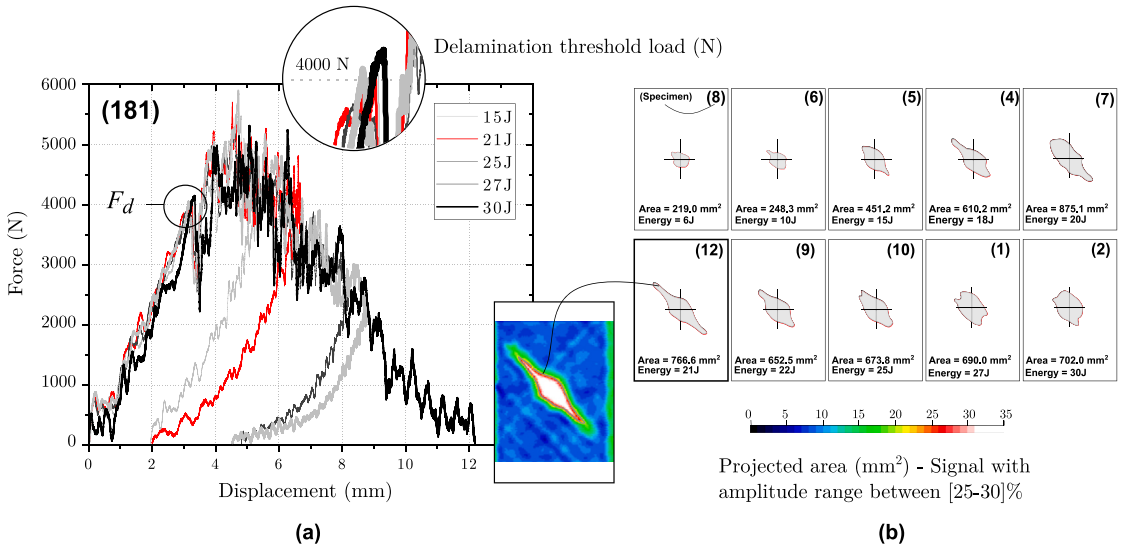

Fig. 4. (a) Impact load evolution in function of displacement for the configuration 181, (b) Projected area profile (configuration 181).

increase and shapes are distorted following an oval pattern with a large aspect ratio and major axis aligned with the fibre orientation of the delaminated ply. This phenomenon is mainly due to the increasing delamination of the back face of the specimen. On the contrary, circular patterns for the projected areas were maintained for the thicker laminate 361. For specimens with full penetration, a perfect circular boundary is shown in the impacted zone. More insights of the projected delamination areas related to the same experimental campaign in conjunction with one analysis of the residual compressive strengths by compression after impact (CAI) can be found in [29].

2.5. Drop-weight impact and compression after impact tests

Records of peak load F_p, delamination threshold F_d and dissipated energy for all configurations of laminates in the LVI experimental campaign are shown in Fig. 6. As expected, the peak load F_p increased by increasing the impact energy for all laminates tested (see Fig. 6(a)). However, there is a maximum peak load value just after the BVID which remained constant independently of the impact energy or impact velocity. This behaviour is clearly illustrated for laminates 351 and 361. Maximum peak load values were found for thicker laminates and quite similar quantitative load response was observed for laminates 252 and 351. In addition, the threshold load F_d remained constant and is influenced mainly by the laminate bending stiffness and fracture toughness in pure mode II, independently of the impact energy and delamination size [41]. This interesting behaviour is shown in Fig. 6(b) for all configurations tested. Finally, the comparison for dissipated energy is shown in Fig. 6(c). Thinner laminates presented the major dissipated energy values, with more notable variability/scatter after reaching the BVID threshold. For lower impact velocity values, F_d can be difficult to determine owing to the governing parameters, or due to harmonic resonances of the (impactor/load cell), or of the specimen during the impact, with F_d even becoming equal to F_p [42]. Laminates 252 and 351 present similar energy dissipation behaviour, associated with their similar material bending stiffness. The thicker, 361 laminate configuration produced the lowest proportion of dissipated energy in which a high percentage of the energy was recovered elastically (see Fig. 6(c)).

In order to address the damage tolerance, CAI tests were performed for all laminates following the standard requirements [38]. A full report of the experimental results with an reliable numerical methodology approach for this particular test campaign can be found in [29]. In this work, three configurations (181, 181T and 252) were selected to illustrate the mechanical behaviour of the residual compressive loads (σ_c). Plotting the residual strength and projected delamination areas as a function of the impact energy, as shown in Fig. 6 (d–f), reveals an interesting trend. It is observed that increasing the impact energy reduces the residual strength for all the laminates tested until reaching an almost constant value. In similar manner, projected delamination areas remain constant for impact energies larger than the BVID threshold, which means that all the energy goes into local crushing and further penetration of the laminate. This behaviour was observed as a general trend for all tested laminate configurations.

3. Constitutive model to predict damage in composite materials

Failure mechanisms for composite laminates are usually divided into two groups, the interlaminar and intralaminar damage behaviour. Interlaminar damages describes the separation between plies which takes place under different crack opening modes. Whereas intralaminar damage behaviour considers all the failure mechanisms which occur within each ply. In this work, both numerical constitutive approaches are used to model the fracture damage modes and their interaction in unidirectional laminates under out-of-plane loading conditions. With regard to the interlaminar damage, it is assumed to occur in the form of delaminations along predefined discrete crack planes and a cohesive zone model (CZM). On the other hand, a continuum damage model (CDM) is applied at ply level to capture different damage mechanisms. These mechanisms mainly occur in the form of fibre breakage and matrix cracking on the impacted zone. By combining both damage models within a sophisticated kinematic modelling approach, matrix cracks and delaminations are predicted realistically. The intralaminar damage model has been implemented in Fortran-coded 'VUMAT' subroutine to be used with an explicit numerically integration scheme. A brief aspects of both constitutive models will be presented as follows.

3.1. Interlaminar behaviour

The interlaminar damage response at interface level is modelled by means of a classical cohesive zone method (CZM) readily available in ABAQUS/Explicit [33], using a native surface-based cohesive-frictional formulation coupled to a penalty contact algorithm [43,44]. Instead of using cohesive-elements which impose mandatory use of regular mesh with coincident nodes location through the thickness, surface-based contact interaction facilitates the use of non-conforming meshes at ply level that can be aligned with the material orientation. The

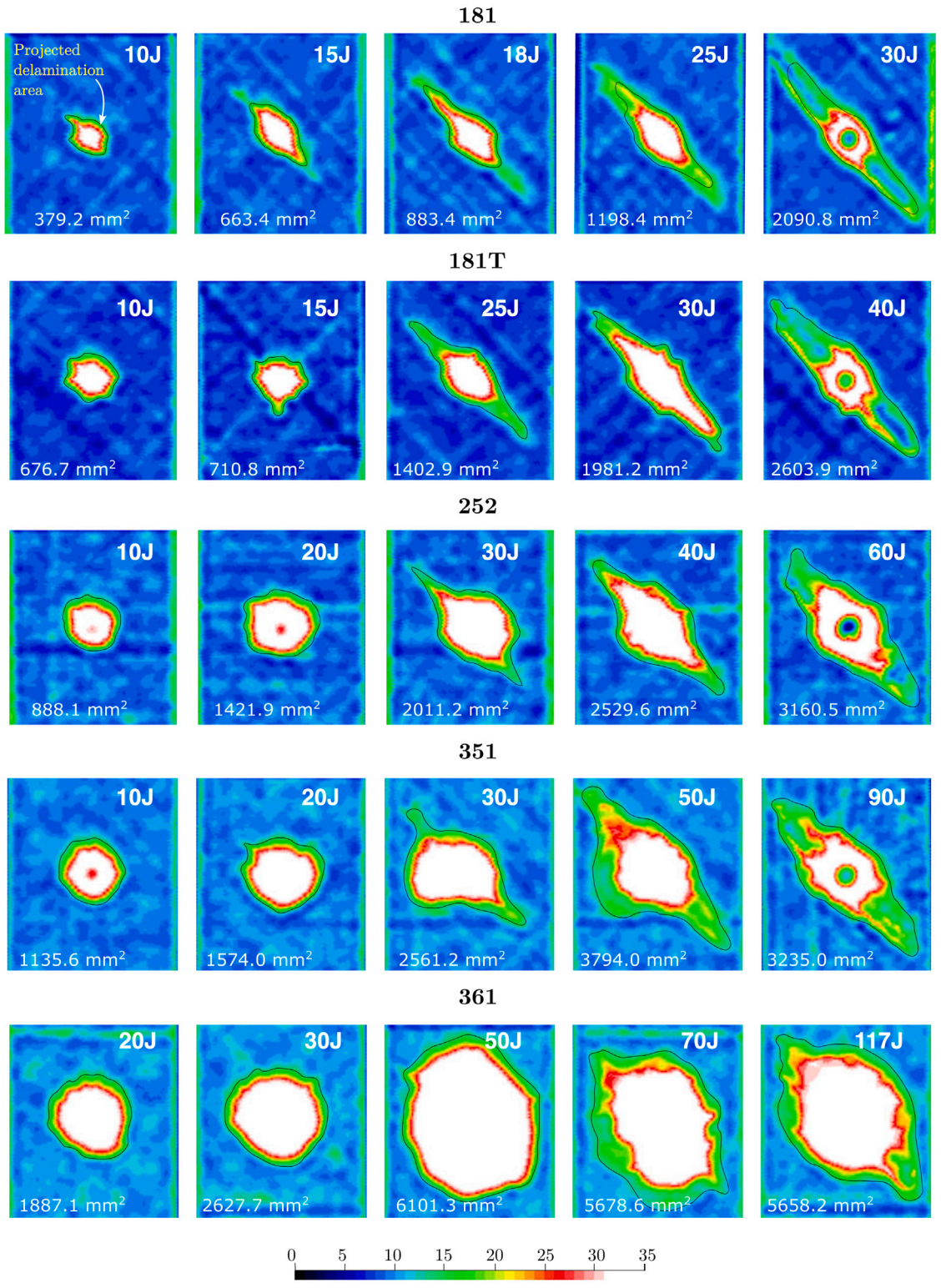

Fig. 5. Profiles mapped by means of Ultrasonic NDT C-scan inspection and projected delamination areas for analysed configurations. The different colours identify the signal amplitude (in %).

surface-contact interaction allows mesh directional biasing with different element sizes by ply according to the computed characteristic element length requirements. Concerning delamination onset, both the ply interface shear strength and the interface normal strength are determined by the interlaminar shear strength (ILSS) test [45] and the value of the transverse tensile strength for a thick embedded ply, adopting the same assumption used in [28].

3.2. Intralaminar behaviour and mesh size regularization

In this work the fibre-reinforced composite material is modelled herein by means of a thermodynamically-consistent continuum damage model (CDM) based on the work of Maimí et al. [34,46] and implemented as Abaqus/Explicit 'VUMAT' user subroutine. This work combines Maimí's formulation with mesh-alignment techniques in order to reduce mesh sensitivity associated with CDM to permit accurate

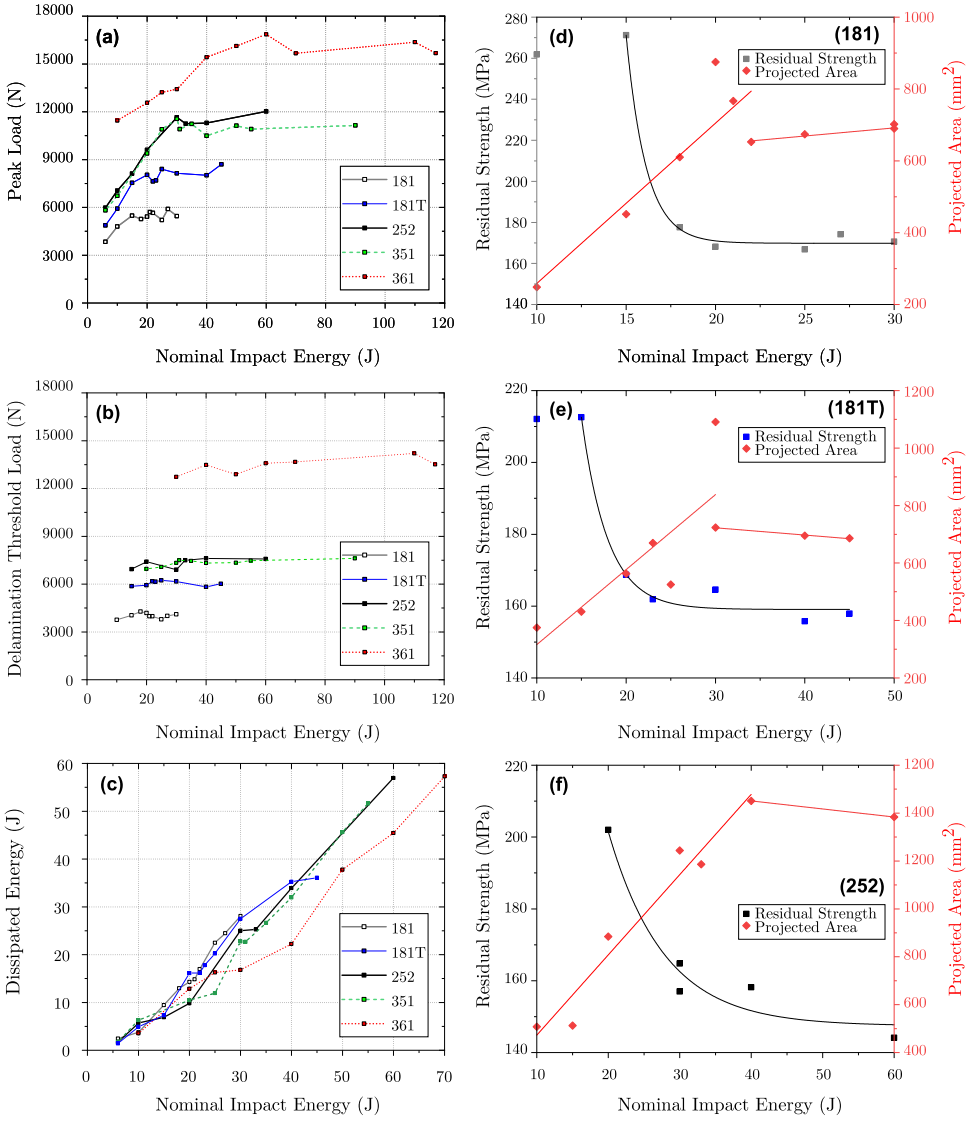

Fig. 6. (a) Comparison of Peak loads F_p, (b) delamination threshold F_d and (c) amount of dissipated energy for all laminates tested. (d,e,f) CAI residual strength (σ_c) and projected area, as function of the impact energy for the configurations 181, 181T and 252 respectively.

crack predictions. The orthotropic damage model follows different elastic behaviour according to the material direction until the first-ply failure is detected by means of physically-based three-dimensional failure criteria developed by Catalanotti et al. [35]. A nonlinear elastic-damageable behaviour was considered for the in-plane and out-of-plane shear response, based on a Ramberg–Osgood law [47]. The gradual unloading of a ply after the onset of damage is simulated by means of appropriate progressive damage evolution laws according to different damage modes.

Exponential stress softening laws describe the damage evolution forms corresponding to fibre kinking and matrix cracking damage expressed in the following general form [46]:

$$d_M = 1 - \frac{1}{f_N\left(r_N\right)} \exp\left\{A_M\left[1 - f_N\left(r_N\right)\right]\right\} f\left(r_K\right) \tag{4}$$

wherein the function $f_N\left(r_N\right)$ force the softening of the constitutive relation and $f\left(r_K\right)$ is the coupling factor between damage laws and elastic threshold domains. The parameter A_M is calculated internally by means of numerical integration to ensure that the computed dissipated energy is independent of mesh refinement. A detailed explanation of this parameter for fibre failure can be found in [28]. In this section only the parameter A_M for matrix failure is described and calculated using the following expression:

$$A_M = \frac{2l_2^* X_M^2}{2E_M \mathcal{G}_M - l_2^* X_M^2}, \; M = 2\pm, 4, 5, 6\,, \tag{5}$$

wherein E_M and X_M are the Young modulus and ply strengths corresponding to each failure mode [48]. $\mathcal{G}_M$ is the energy release per unit volume and l^* is the element characteristic length and represents a typical cracking distance across the surface of an element [49]. The mesh regularization follows the scheme proposed by Bažant and Oh [36] which assure the objective solutions, i.e. guarantees that $l^* g_M = \mathcal{G}_M$, For square elements with an aspect ratio approximately equal to one, the characteristic element length can be approximated by [36]: $l_1^* = l_2^* = l^* = 1.12\sqrt{A_{IP}}$, wherein and A_{IP} is the area associated with an integration point projected in the plane of crack propagation.

For the material-aligned meshing approach used in this work, two independent characteristic lengths, $l_{1,max}^*$ and $l_{2,max}^*$ were taken into account (see Fig. 8). The maximum element size that guarantees the correct representation of both material strength and fracture energy dissipation simultaneously can be computed using the following general

expression from Bažant's crack band model [36]:

$$l^*_{1,max} = min\{\frac{2E_1\mathcal{G}_M}{X^2_M}\},\ M = 1+, 1- \tag{6}$$

and

$$l^*_{2,max} = min\{\frac{2E_i\mathcal{G}_M}{X^2_M}\},\ M, i = 2\pm, 4, 5, 6 \tag{7}$$

3.3. Physically-sound crack simulation by element erosion techniques

One of the most generalized techniques for modelling crack propagation in composite materials is the use of element erosion. In this work element erosion is combined with both CDM and CZM damage models for modelling realistic cracks patterns. This technique has the benefit of being able to simulate cracking phenomena through a simple and efficient algorithm in which elements are removed automatically once they reach complete failure by a predefined criterion. In this work, the element erosion approach is combined with material-aligned meshes. This, allows the simulation of material cracks in the strong sense i.e. with kinematic discontinuities between crack faces. Once an element is removed from the mesh, penalty-based frictional contact conditions are enforced at the free faces of the neighbouring elements to model the crack faces, avoiding interpenetration and allowing stress transfer in case of crack closure. In addition, this approach helps avoid excessive element distortions which would introduce spurious effects in the computation of stresses reducing the efficiency of the analyses. Furthermore, element erosion is a native algorithm implemented in several solvers like Abaqus or LS-DYNA. [33]

Despite of the benefit mentioned above, some drawbacks can be pointed out. One of the most important is that it leads to the undesired loss of volume, mass and potentially available energy from the system including poor load bearing capability mainly during contact interactions. Although in CDM the crack separation is smeared over a characteristic length that guarantees the correct representation of both material strength and fracture energy dissipation. In general, the characteristic length is found to be on the order of less than 1 mm in all three spatial dimensions. This imposes an expensive computational cost for large models. One other important disadvantage of eroding elements in the smeared-damage crack band is that crack faces are generated at a relative distance between each other, corresponding to the finite thickness of the crack-band. One of the consequences of this is mitigated by the fact that stresses around a crack need a finite distance to recover to nominal values, according to a shear-lag assumption. The second consequence of crack-band erosion would only have an effect on compressive and shear dominated cracking. Finally, the element erosion technique is a mesh-dependent solution and requires more complex procedures for automated aligned-mesh generation, in order to enforce damage localization along physically-sound crack paths, specially when matrix crack are the dominant damage mode [50]. Aligned-meshing strategies have been used by previous authors for low and high velocity impact simulations with manual or semi-automated mesh generation operations [25,27,51,52]. In this work a fully automated aligned-mesh generator was implemented by means of the programming language Python using ABAQUS-scripting commands and in-house python modules (see Fig. 8). Following the same procedure by the authors in [27] in order to model opening cracks, element erosion is enforced when d_{1+} or d_{2+} reach values close to unity. In addition, highly distorted elements are avoided by setting limits on the determinant of the deformation gradient (det **F**). This variable is defined as the ratio between the deformed (V) and undeformed (V_0) volumes of an element [27].

4. Virtual testing set-up for low-velocity impact and material properties

In order to guarantee high fidelity-simulations, two key aspects for the meso-scale modelling discretization were considered: The kinematic modelling approach and the material input properties. In this section both aspects will be briefly described. Related to the numerical strategy applied in the virtual laboratory for LVI, the same modelling approach was used by the authors for quasi-static in-plane loading cases [27] and in the present work is adapted to out-of-plane dynamic loading conditions.

4.1. Modelling set-up

The FE model setup is simulated following similar requirements as the ones indicated by the AITM1-0010 test standard described in Section 2. The geometry and boundary conditions of the analysed models are shown on Fig. 7. Four main features (fixture-base, laminated-composite, clamps and impactor) are included to build up the assembly. Laminate test specimens of 150 ×100 mm are fixed between the fixture-base of 200 × 150 mm with a cut-out 125 × 75 mm (to guarantee the specimens impact deflection) and four rubber clamps. Both the base and clamps are modelled as perfectly fixed rigid bodies discretized with R3D4 (2 × 2 mm) rigid elements using hard contact interaction with the specimens. The impactor is modelled as a rigid body with a lumped mass value (M_i) of 5.745 kg. It has a hemispherical-shaped impact surface with a radius (r_i) of 8.0 mm and height (h_i) of 10.0 mm discretized by R3D4 three-dimensional rigid elements with four nodes. An initial velocity (v_0) in the vertical direction is prescribed to the impactor, simulating the impact velocity measured during the analysis. Whereas a gravitational force is applied to the impactor and determined by ($M_i g$).

All specimens where modelled using three zones (i—Damage, ii—Smooth transition and iii—Composite layup zone) with two different levels of discretization in order to optimize computational resources and ensure the localization of failure mechanisms in the central sections. Each laminate ply is discretized by means of a structured aligned meshing technique with one solid homogeneous element (C3D8R and C3D6 solid elements with reduced integration and enhanced hourglass control [53]) through-the-thickness which respond according to the CDM previously described in Section 3.2 and illustrated on Fig. 8. In the central damage zone, structured aligned meshes are extended until the specimen free edges in order to facilitate further compression after impact (CAI) analyses after the impact simulations. For all simulated cases the length of the damage zone need to be large enough in order to include the failure mechanisms that takes place during the analysis. In regions away from the impact described as 'support parts' related to the composite layup zone, only the elastic behaviour is simulated by means of a single layer of coarse continuum shell elements (SC8R) with one integration point per ply that models the whole laminate. Between these two zones, in order to avoid spurious damage due to unrealistic stress oscillations, stress softening is prevented in plies and interfaces in a smooth transition zone close to the kinematically constrained regions. The three regions with different discretizations are kinematically constrained to enforce continuity of displacements and rotations across their boundaries using surface-base tie constraints. In addition, zero-thickness ply interfaces are modelled by means of a surface-based cohesive-frictional formulation coupled to a penalty contact algorithm, as explained in Section 3.1 (see Fig. 8).

4.2. Material input properties

In this work, all LVI coupons are manufactured using unidirectional carbon fibre pre-preg tape, HexPly AS4/8552, supplied by Hexcel with nominal ply thickness of 0.184 mm. The constitutive AS4/8552 average ply properties used as input data for the damage model described

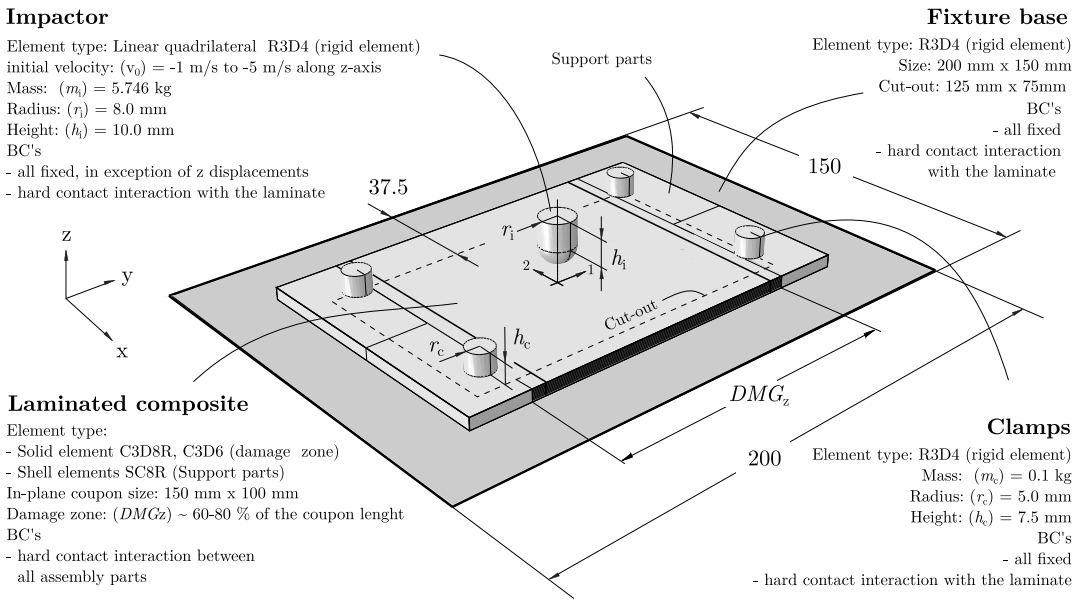

Fig. 7. Modelling set-up for low velocity impact.

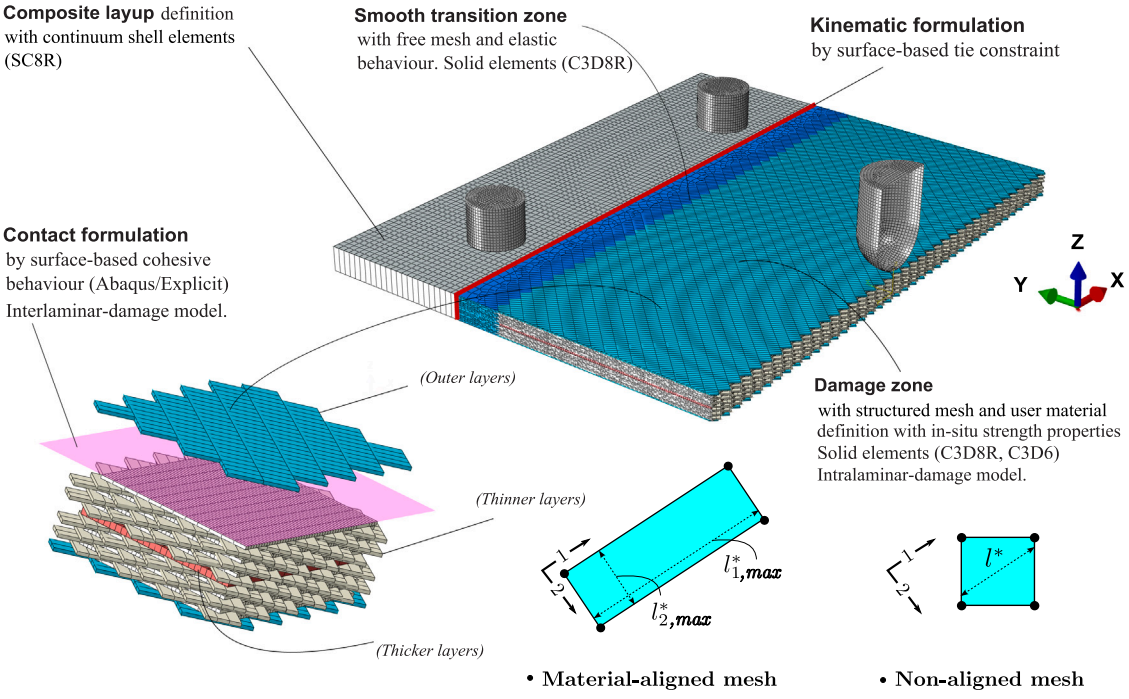

Fig. 8. Low-velocity impact FE model showing structured aligned meshes strategy taking into account the characteristic element length l^*. Damageable zones with cohesive-frictional contact surfaces and material *in – situ* properties are highlighted.

above are reported in Table 2. A detailed description for each material property as well as their interaction with the material model used is presented by the authors in [27,28]. These properties were obtained through an extensive experimental campaign to provide material design allowable values for laminate configurations commonly used to design and certify aircraft structures [54,55] and from available data reported in the literature review. Slightly different values for these properties are reported by NCAMP [55].

Although the material response presents inherent dependency on different strain rates. In this study, only quasi-static material property values have been used. However, previous research on the rate-dependent behaviour of CFRPs has shown that this effect is most important for the strength properties, with the effect on the elastic properties far less pronounced [56]. In addition, in LVI test cases, the laminate response is expected to be dominated by the damage evolution rather than the initiation and there is no clear consensus on whether or not strain-rate significantly affects the fracture toughness properties of CFRPs, especially in the mode II [57,58]. Conversely, Wang et al. [59] showed that strain-rate effects may in fact play an important role for higher energy LVI tests, resulting in greater delamination areas due to the higher rigidity of the laminate at high strain-rates. Therefore, the omission of strain-rate effects in the present work should not be a major cause for concern but may be considered as a potential improvement to the current model in future work.

Table 2
Average material properties used as inputs for the ply and interface model for HexPly AS4/8552 unidirectional prepreg CFRP with density $\rho = 1.58 \cdot 10^{-6}$ kg/mm^3 and nominal ply thickness t_p=0.184 mm. Material properties were taken from [27].

Property	Mean (CV %)
Ply elastic properties	
E_{1t}(GPa)	137.1 (1.4)
E_{1c}(GPa)	114.3 (0.9)
E_{2t}(GPa)	8.8 (0.3)
E_{2c}(GPa)	10.1 (0.8)
$G_{12} = G_{13}$(GPa)	4.9 (0.8)
$\upsilon_{12} = \upsilon_{13}$	0.314
υ_{23}	0.487
Ply strengths properties	
X^T(MPa)	2106.4 (8.2)
X^C(MPa)	1675.9 (5.2)
Y^T(MPa)	74.2 (6.3)
Y^C(MPa)	322.0 (1.7)
S^L(MPa)	110.4 (1.3)
Thermal expansion coefficients	
α_1(°C^{-1})	$0.21 \cdot 10^{-6}$
α_2(°C^{-1})	$3.30 \cdot 10^{-5}$
Ply fracture energies	
$\mathcal{G}_{1+}$(kJ/m^2)	125.0
$\mathcal{G}_{1-}$(kJ/m^2)	61.0
$\mathcal{G}_{2+}$(kJ/m^2)	0.30
$\mathcal{G}_6$(kJ/m^2)	0.87
Interface properties	
τ_3^0(MPa)	74.2
τ_{sh}(MPa)	110.4
$G_{Ic,\theta=0°}$(kJ/m^2)	0.30 ± 0.01
$G_{IIc,\theta=0°}$(kJ/m^2)	0.87 ± 0.06
η_{bk}	1.45

5. Validation of the modelling approach

One of the challenges for virtual testing is not only accurately predicting the material strength and displacements, but also capturing the different failure mechanisms for both damage resistance and damage tolerance respectively. In order to validate the implemented modelling approach, several numerical simulations were performed for impact energy values above and below the BVID threshold. In addition, simulations for all BVID energy thresholds were included and validated against the experimental data.

5.1. Numerical predictions of the damage due to low-velocity impact

In this section, numerical simulations of LVI using the previously described high-fidelity FE model are correlated with experimental results reported in Section 2. During the simulation campaign, the main items analysed for validation and comparison were: realistic intralaminar/interlaminar failure prediction, projected delaminated areas, impact peak-loads, impactor displacements, impactor velocity and dissipated impact energy.

The response depicted in Fig. 9(a) predicts the evolution of macroscopic failure mechanisms during the LVI simulation, up to laminate perforation for the laminate 181 impacted at 30 J above a BVID threshold of 21 J. It is clearly seen that the damage takes place throughout the thickness by means of matrix cracking and delaminations, being more visible for higher impact energy values. Above BVID the fibre splits extend towards the edges and may even entirely detach from the coupons. This material behaviour was correctly captured during the simulation. A macroscopic observation of failure mechanisms after the impact is shown in Fig. 9(b). At this impact energy value with full penetration, in the non-impacted face, large fibre splitting and matrix cracking oriented at 45° were observed. Whereas, in the impacted face of the specimen, significant damage with fibre breakage was concentrated mainly in the impact location. In comparison with the experimental results, these intralaminar and interlaminar failure mechanisms were accurately predicted during the numerical analysis and are illustrated in Fig. 9(c). A cutting plane $A - A'$ is used to observe the predicted catastrophic failure through the thickness. In addition, a strong interaction between matrix cracks and delaminations was found, particularly for $\mp 45°$ ply interfaces. At the ply level, matrix cracks create stress concentrations that physically interact with interlaminar damage failure and guide the delaminations to propagate. This phenomena was realistically captured during the simulation.

Another simulated example for a specimen impacted with an energy value above the BVID threshold, but without full penetration is illustrated in Fig. 10. This example is the laminate 351 impacted at 55 J with a BVID threshold of 35 J. On the left side, a macroscopic view of the damage for both impacted and non-impacted faces for the main intralaminar failure mechanisms and permanent indentation around the impact point is shown. Next, the internal interlaminar damage obtained by NDT C-scan inspection is revealed. In general, like the previous laminate 181 described before, the first significant failure mechanisms were located at the back faces and were realistically predicted. The damage resistant behaviour is produced mainly owing high tension and shear matrix cracks in the structure. The predicted intralaminar failure response was compared with the visible damage failure from outside the specimen with high agreement for both, the impacted and back faces. At this impact energy value, intralaminar damage becomes visible even from the outside in the form of matrix cracks and of fibre breakage. Whereas for the interlaminar damage response, predicted delamination areas (see dashed contour profile) were compared against the projected delamination areas inspected by C-scan. The 3D modelling approach was able to qualitative predict the shape of the delamination area in similar fashion. In addition, the interaction between matrix cracking and delaminations was accurately captured in the simulation.

For impact energy values below the BVID threshold, internal damage mechanisms are extremely difficult to detect by visual inspection and more sophisticated technology needs to be employed, such as NDT C-scan or computed tomography (CT) inspection methods. However, by

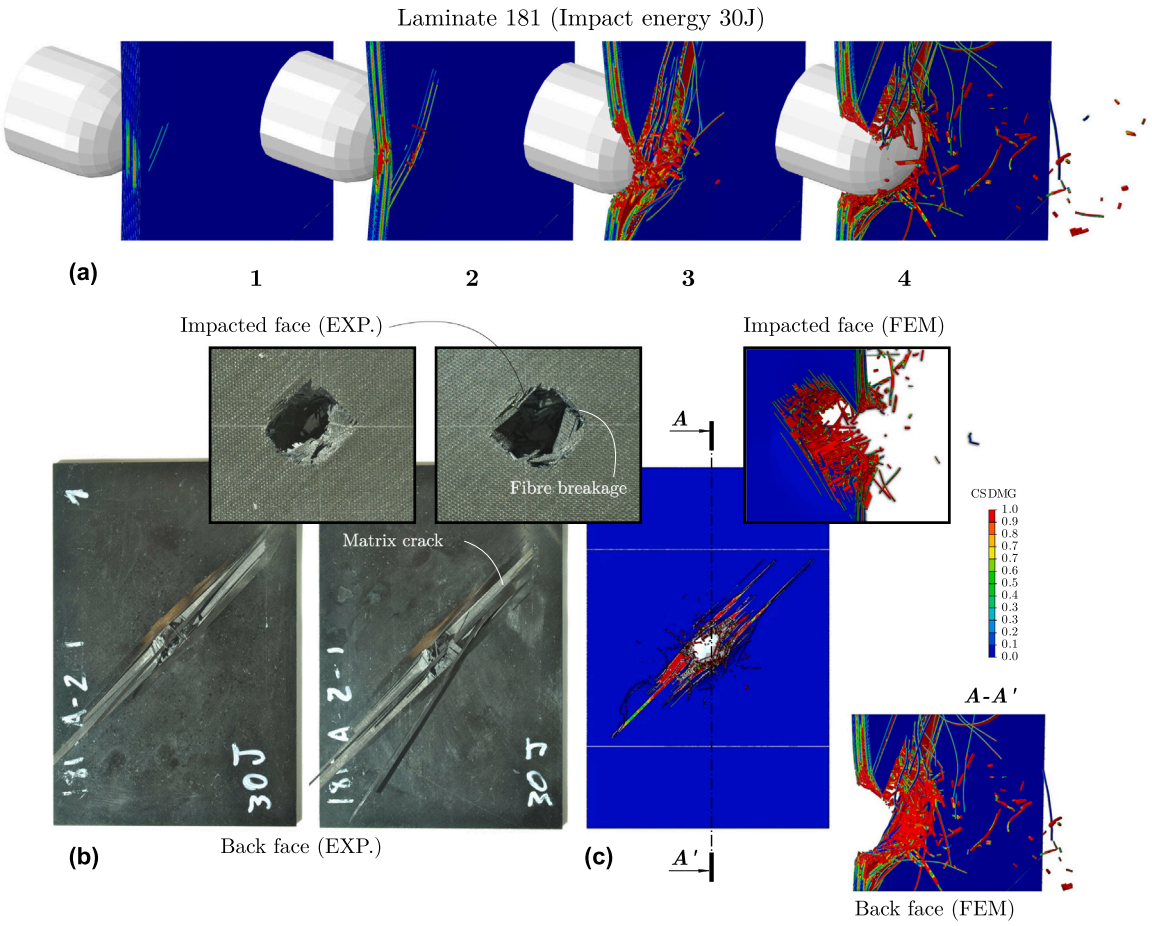

Fig. 9. (a) Evolution for both intralaminar and interlaminar damage for laminate 181 impacted at 30J, (b) Macroscopic observation of failure mechanisms of specimen with full penetration at 30J and (c) Predicted (macroscopic) failure mechanisms.

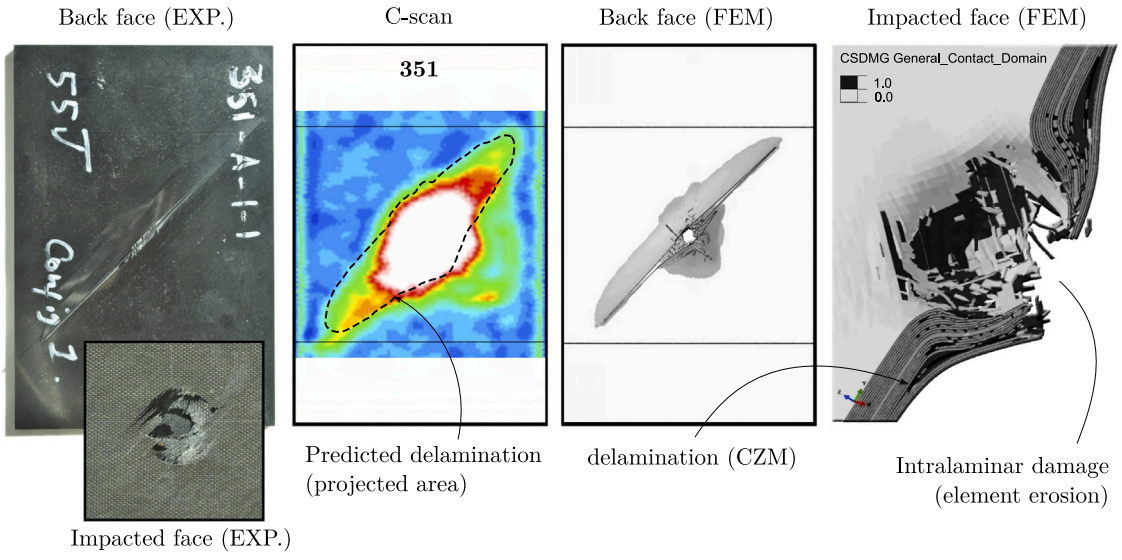

Fig. 10. Delamination areas of the laminate 351 for impact energy 55 J (comparison between experimental (C-scan) and numerical (dashed line).

using high-fidelity simulations, more insight into the internal damage mechanisms for the material behaviour can be virtually replicated. Fig. 11(a) illustrates the evolution of the material response for laminates 252 and 361 impacted with energy values below BVID at 30 J and 50 J respectively. The response is governed by the flexural and shear waves which propagate from the impact point to the plate boundaries and through the contact forces between the impactor and the laminate. At this impact energy level, the major delamination areas predicted by in the simulation were located around the mid-plane of the specimen due to the high interlaminar shear stresses that are concentrated in this zone. By increasing the contact time and impact forces, delaminations eventually migrate to the upper and lower interfaces. Although barely

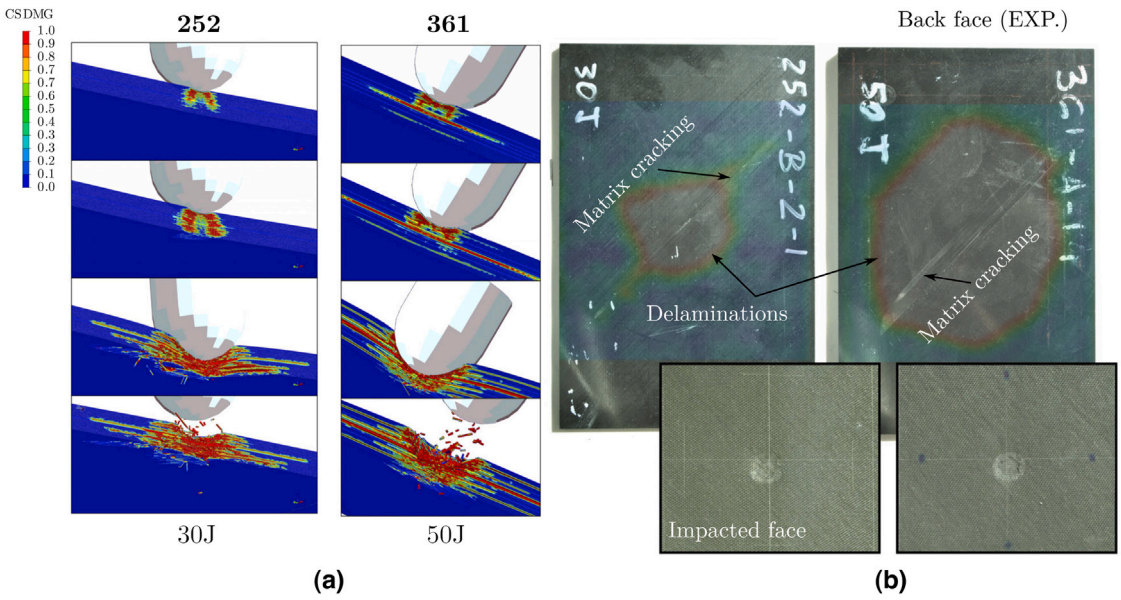

Fig. 11. (a) Cutting view of a drop-weight impact simulation for laminates 252 and 361 with impact energy values of 30J and 50J respectively. (b) Samples of specimens impacted with permanent indentation.

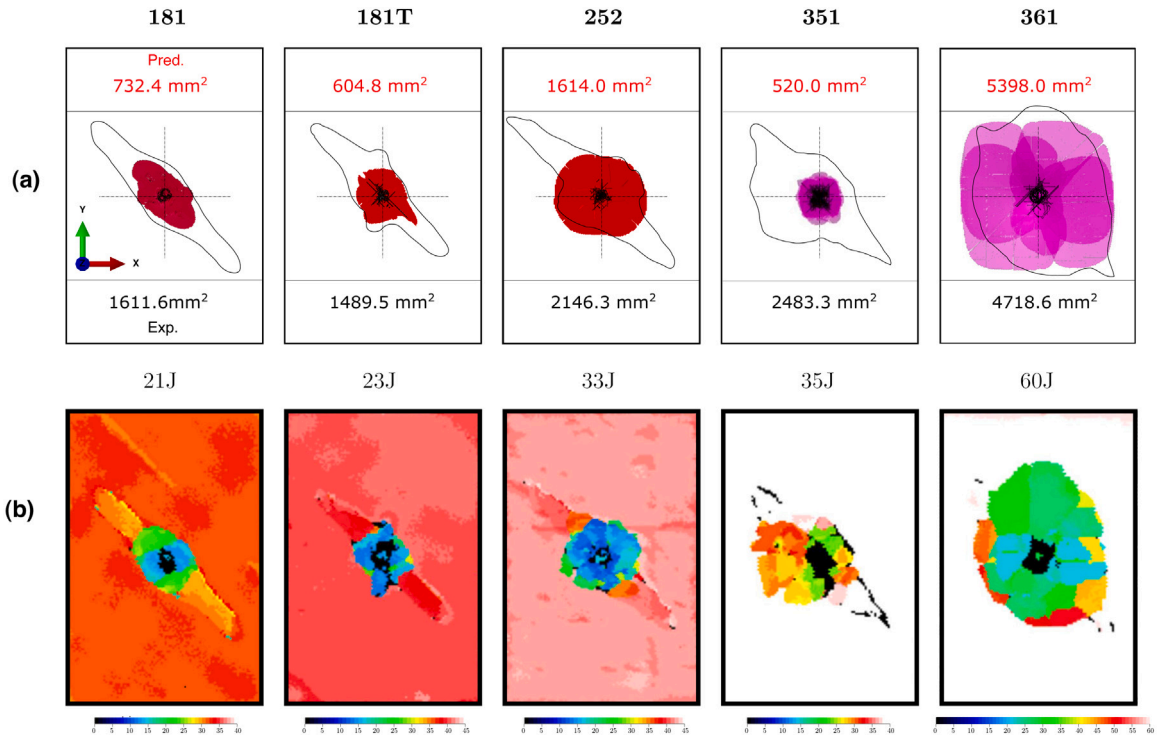

Fig. 12. Comparison of (a) simulated and (b) experimentally-obtained delamination areas for each laminate configuration impacted at the corresponding BVID Energy threshold [29]. The colour scheme identify the depth of delamination (scale: ×0.1 mm).

visible singular cracks were observed on the non-impacted faces during the experiments (see Fig. 11(b)), the 3D modelling was unable to accurately capture these cracks. In both cases during the drop-weight impact test, the impactor rebounded back and a percentage of the energy was recovered elastically. In addition, permanent indentations remained for both laminates after the impact and was captured during the simulation.

Finally, the NDT depth scan damage inspection data and the corresponding predictions of the projected delaminations areas for all analysed configurations impacted at BVID energy threshold are compared in Fig. 12. For comparison purposes, from the 3D-scan only the outer contour resulting of the superimposition of delaminations at different interfaces was used. In general, the global shape of the delamination areas for the other laminates differ from the real ones and they tend to be under predicted. At this impact energy value the modelling approach was unable to capture the typical fibre splitting located at the non-impacted face that produces a large delamination oriented along the ply angle. Only for the particular cases of the

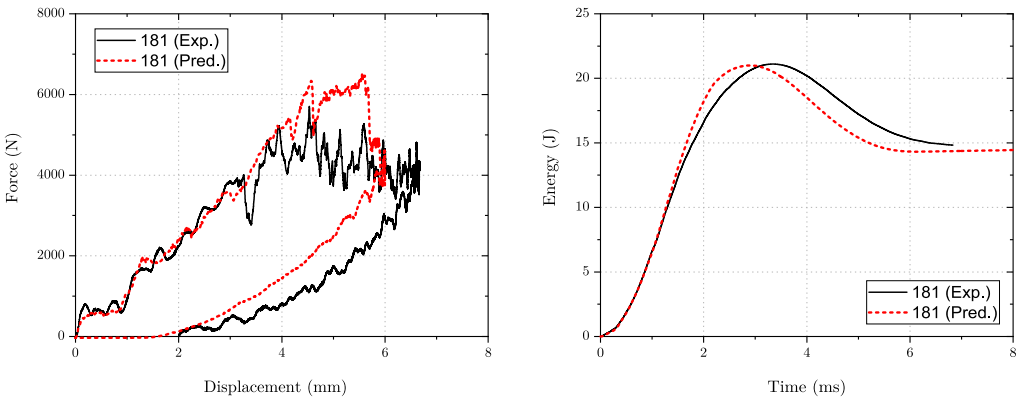

(a) Laminate 181 (BVID Energy threshold 21J)

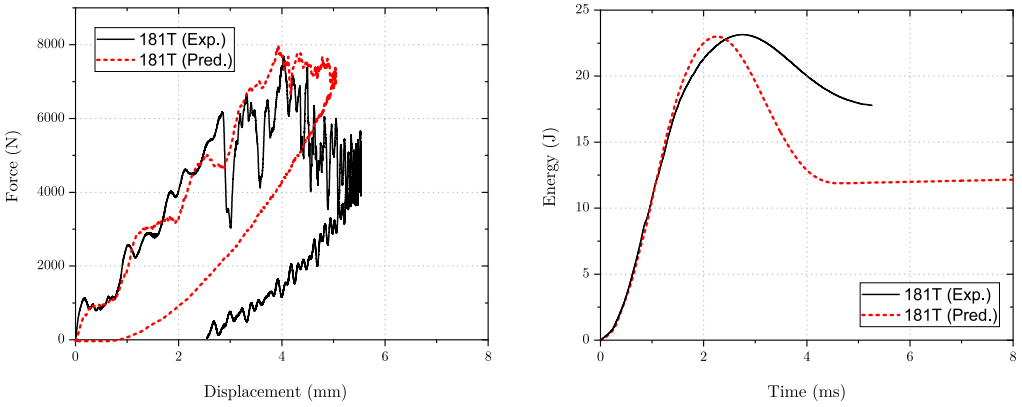

(b) Laminate 181T (BVID Energy threshold 23J)

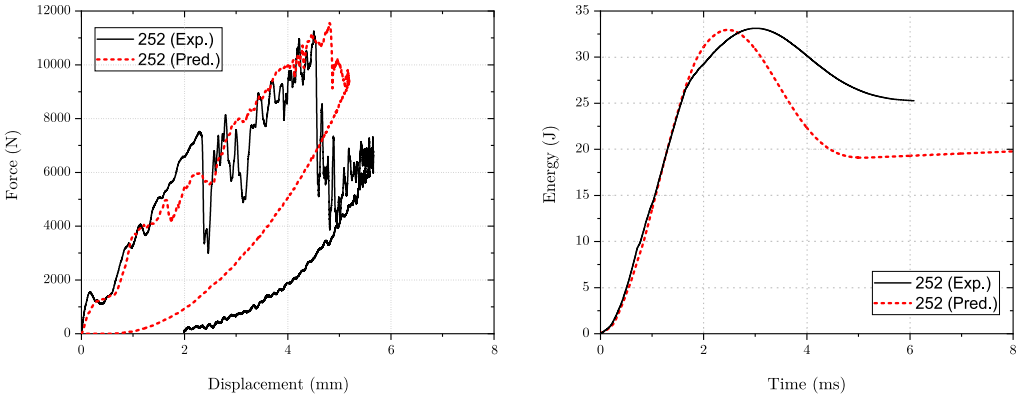

(c) Laminate 252 (BVID Energy threshold 33J)

Fig. 13. LVI predictions and comparisons with experimental data: Impact load in function of displacement and evolution of the absorbed (BVID Energies threshold) (a) laminate 181 impacted at 21 J; (b) laminate 181T impacted at 23 J; (c) laminate 252 impacted at 33 J. All the results are shown without filtering.

thicker laminate 361, with circular shape of the delamination area was observed and accurately predicted by the FE model. One explanation for this effect could be related with the criteria used to erode elements and the high value used for the penalty stiffness parameter K (see Section 3.1, 3.3). Another reason could be an under prediction of the damage evolution because strain-rate effects were not taken into account. In a study by Wang et al. [59], it was shown that including rate effects on the strength and stiffness properties resulted in greater predicted delamination areas due to the greater rigidity of the laminates for LVI test cases at high impact energies. Therefore, this should be considered in future work to improve the quality of the predictions. From the point of view of the authors, more rigorous model calibration needs to be performed in order to improve the simulation results for general impact scenarios.

5.2. Force–displacement, energy dissipation and velocity predictions

A comparison between the experimental data (Exp.) and numerical simulations (Pred.), of impactor reaction force histories, evolution of the absorbed energies and impactor velocities for all laminates tested with BVID energy values, are plotted in Figs. 13–15. In general it can be observed that curves follow similar trends in terms of global response and contact times. However, in order to evaluate the accuracy of the simulations, some differences are worth mentioning. From the experimental tests, an oscillatory behaviour due to the dynamic

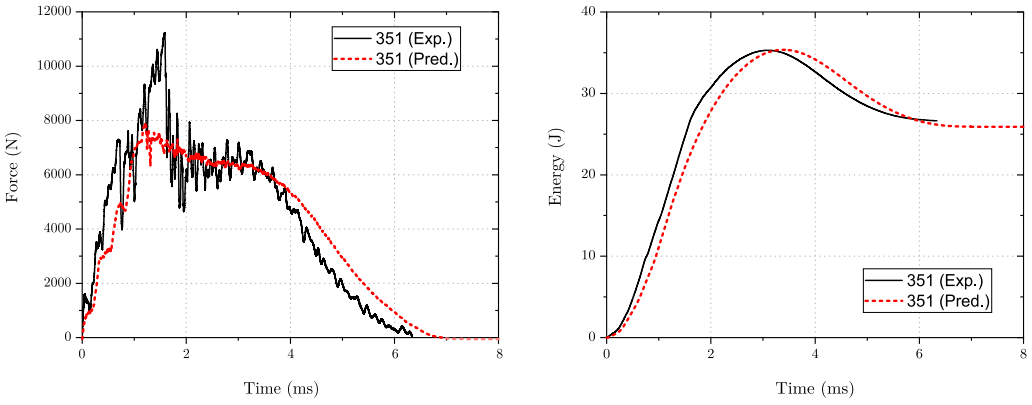

(a) Laminate 351 (BVID Energy threshold 35J)

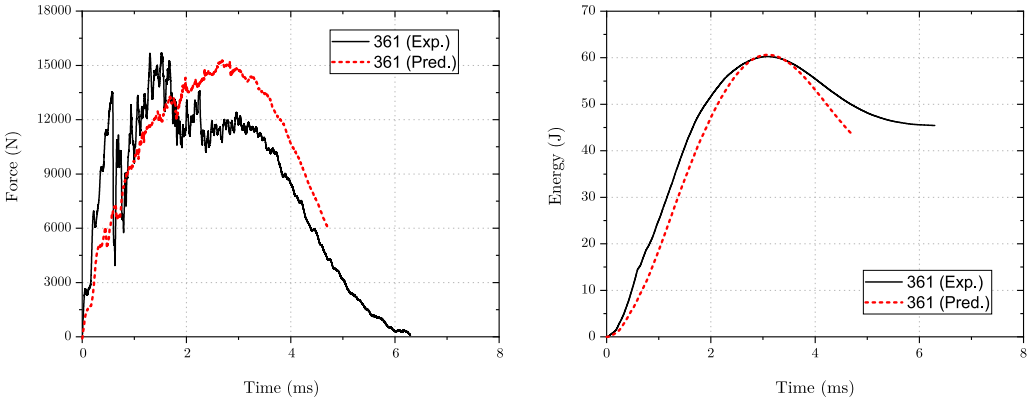

(b) Laminate 361 (BVID Energy threshold 60J)

Fig. 14. LVI predictions and comparisons with experimental data: Impact load and absorbed energies evolution (BVID Energy threshold) (a) laminate 351 impacted at 35 J; (b) laminate 361 impacted at 60 J. All the results are shown without filtering.

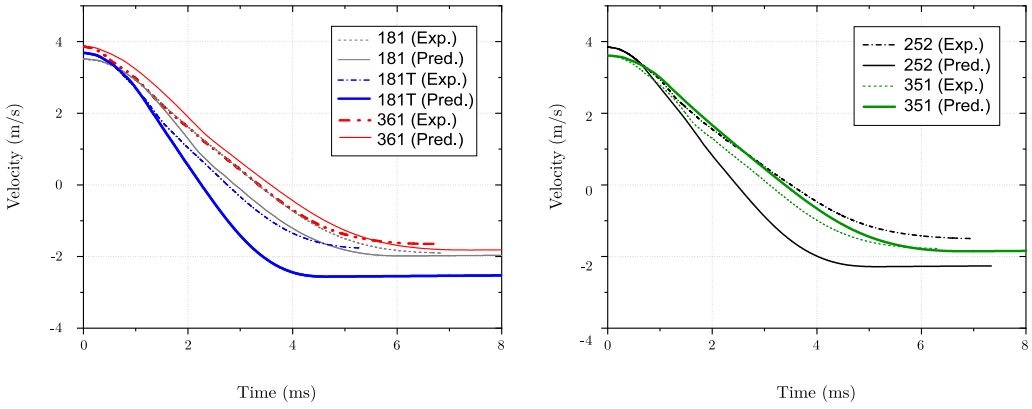

Fig. 15. Velocity histories for laminates impacted at BVID energy. Laminate 361 impacted at 70 J.

coupling between the specimen and its base-support was observed, but this phenomenon was not correctly replicated by the simulations. This provokes unrealistic viscous dissipation mechanisms that damped the dynamic responses of the systems. In addition, while clear delamination thresholds, F_d, were unable to be predicted from the numerical model results, the laminate response up to the peak load, F_p, appears to be relatively accurate for the low energy impacts. This indicates that the lack of strain-rate effects in the material strength properties may not be a crucial factor in these test cases. However, as the laminate thickness and impact energy increase, it appears that the predicted strength and stiffness of the laminate begin to deviate more significantly from the experimental results. This is in line with the results from Wang et al. [59], which showed that the effects of strain rate on the strength and stiffness become more important at higher energy impacts.

The most favourable predictions was made for the laminate 181. However, the behaviour is less well predicted for the other laminates. In terms of material stiffness for the other laminates, the initial stiffness of the specimens is higher than the simulated, particularly for the laminates 351 and 361. This is because the progressive fibre breakage mechanisms were over-predicted. In addition, after the peak load F_p, the elastic recovery of the laminate is slightly over predicted in most cases, as indicated by the drop in absorbed energy during the unloading/rebound stage. This inaccuracy in the numerical results was observed mainly for the laminates 181T and 252 and clearly illustrated

Table 3
Summary of computational cost of the LVI simulations run on Intel Xeon (16/20-core) computing nodes. Element size: approximately 0.6 ×0.2× 0.184 mm. The analysis time period was 8 ms with a stable time increment of approximately 1.6×10^{-8} s.

Model	Impact energy [J]	Elements [$\times 10^3$]	Nodes [$\times 10^3$]	DoF [$\times 10^3$]	Increments [$\times 10^3$]	CPUs	Wallclock time [h]
181	21	789	1572	4717	515	64	22
	27				516	64	22
181T	23	1346	2691	8073	530	64	43
	30				533	64	43
252	33	1626	3258	9773	579	60	90
	40				568	60	88
351	35	1346	2691	8073	533	64	43
	55				536	64	44
361	60	1767	3540	10621	342	60	60[†]
	70				541	60	101

Partial results: [†]4.8 ms

in the comparison of impactor velocities in Fig. 15. However, for the other laminates, the velocity histories were well replicated by the numerical model. By analysing the unloading curves of these two laminates, the permanent indentation values owing to the intraply frictional resistance and fibre/matrix failure under shear loads, were underpredicted. For the other tested laminates, both the energy dissipation and the predicted indentation are in good correlation with experimental results.

5.3. Computational cost analysis

The computational cost of the meso-scale CDM-based progressive failure approach can be quite expensive. For this simulation campaign, virtual tests where performed using High Performance Computing (HPC) and the FE models are parallelized on a cluster composed of a group of three and four linked computing nodes: Intel Xeon IvyBridge 2.5 GHz CPU's with 16 or 20-cores each. Several items are negatively influencing the computational cost: (i) light, stiff material reduces the stable time increment, (ii) small element size required to ensure appropriate energy release increases the number of elements and decreases the time increment, and (iii) large number of elements for ply-by-ply modelling. The element size was $0.6 \times 0.2 \times 0.184$ mm (longitudinal × transverse × thickness). The simulated time period was 8 ms and the time increment was approximately 1.6×10^{-8} s. The analysis was carried out with Abaqus/Explicit 6.13-3 with the double precision executable. The computational costs, along with model statistics, are summarized in Table 3 for all configurations.

6. Conclusions

The presented work demonstrates the capability of the virtual testing framework to accurately predict the damage and failure mechanisms in composite laminates under low-velocity impact loading. The robustness of the implemented meso-scale methodology to perform reliable virtual testing of multi-directional laminates by extending the initial in-plane virtual testing to new scenarios of cases under dynamic impact loading, without performing any tuning or calibration processes of the input parameters is displayed. In addition, the methodology is validated through an extensive experimental campaign which embraces not only a wide range of cases with different layup configurations, but also several impact energy values and cases with full penetration with high interaction of damage mechanisms. This large design-space of cases for validation includes several examples to predict physically the complexity of the impact events, the structural behaviour and loading, contact interactions, friction, damage and failure. From the experimental results it is concluded that increasing the impact energy, the maximum impact force F_p are increased, whereas the threshold load, F_d, remains constant. In addition, for impact energies beyond BVID, both the projected delamination area and the residual strength reach an almost constant value independently even though impact energy levels increase. For the numerical methodology, a nonlinear FE modelling and simulation strategy that takes into account the *in-situ* material properties and uses regularization to reduce mesh dependency has been implemented. In addition, the combination of both physically-based constitutive damage models and kinematic modelling with material aligned meshes ensures the simulation of failure mechanisms, permanent indentation and the correct dissipation of fracture energy with high realism.

Although the numerical simulations were not able to capture the unstable delamination growth and sudden drop in force at the delamination threshold, the predictions of the maximum impact load and the damage mechanisms revealed good agreement with the experimental data. The evolution of the energy dissipated, laminate displacement and the projected delamination area, were for some cases underpredicted, mainly for BVID impact cases. This could be related to the drawbacks of the element erosion technique used as well as the interaction of both interlaminar and intralaminar damage mechanisms during fibre splitting. However, in general, the macroscopic failure modes are very well predicted. The methodology may be further improved in future work by considering strain-rate effects in order to extend the capabilities to high velocity impact events. In general, the virtual testing framework constitutes a powerful tool to support in the development of new composite materials and design of composites structures in the transportation sector.

CRediT authorship contribution statement

O. Falcó: Conceptualization, Methodology, Software, Investigation, Validation, Writing – original draft. **C.S. Lopes:** Conceptualization, Methodology, Software, Supervision. **D.E. Sommer:** Writing – review & editing. **D. Thomson:** Writing – review & editing. **R.L. Ávila:** Writing – review & editing. **B.H.A.H. Tijs:** Project administration, Resources, Methodology, Software, Writing – review & editing.

Declaration of competing interest

The authors declare that they have no known competing financial interests or personal relationships that could have appeared to influence the work reported in this paper.

Data availability

The raw/processed data required to reproduce these findings cannot be shared at this time as the data also forms part of an ongoing study.

Acknowledgements

This paper is dedicated to the memory of our dear colleague and friend C.S. Lopes. The research leading to the developments described was funded within the framework of the project VIRTEST (Multiscale Virtual Testing of CFRP Samples), a collaboration between IMDEA Materials Institute and GKN Aerospace: Fokker. The main author is grateful to the collaboration of members from the Impact Engineering Laboratory (IEL) in the University of Oxford for their valuable commentaries in this work.

References

[1] Reiner J, Zobeiry N, Vaziri R. A stacked sublaminate-based damage-plasticity model for simulating progressive damage in composite laminates under impact loading. Thin-Walled Struct 2020;156:107009.
[2] González EV, Maimí P, Martín-Santos E, Soto A, Cruz P, De La Escalera FM, de Aja JS. Simulating drop-weight impact and compression after impact tests on composite laminates using conventional shell finite elements. Int J Solids Struct 2018;144:230–47.
[3] Lopes C, Camanho P, Gürdal Z, Maimí P, González E. Low-velocity impact damage on dispersed stacking sequence laminates. part II: Numerical simulations. Composites Sci Technol 2009;69(7–8):937–47.
[4] Bogenfeld R, Kreikemeier J, Wille T. Review and benchmark study on the analysis of low-velocity impact on composite laminates. Eng Fail Anal 2018;86:72–99.
[5] Soto A, González E, Maimí P, n de la Escalera FM, Sainz de Aja J, Alvarez E. Low velocity impact and compression after impact simulation of thin ply laminates. Composites A 2018;109:413–27.
[6] González E, Maimí P, Camanho P, Turon A, Mayugo J. Simulation of drop-weight impact and compression after impact tests on composite laminates. Compos Struct 2012;94(11):3364–78.
[7] Tan W, Falzon BG, Chiu LN, Price M. Predicting low velocity impact damage and Compression-After-Impact (CAI) behaviour of composite laminates. Composites A 2015;71:212–26.
[8] Bouvet C, Castanié B, Bizeul M, Barrau J-J. Low velocity impact modelling in laminate composite panels with discrete interface elements. Int J Solids Struct 2009;46(14–15):2809–21.
[9] Bouvet C, Rivallant S, Barrau J-J. Low velocity impact modeling in composite laminates capturing permanent indentation. Composites Sci Technol 2012;72(16):1977–88.
[10] Shi Y, Swait T, Soutis C. Modelling damage evolution in composite laminates subjected to low velocity impact. Compos Struct 2012;94(9):2902–13.
[11] Hongkarnjanakul N, Bouvet C, Rivallant S. Validation of low velocity impact modelling on different stacking sequences of CFRP laminates and influence of fibre failure. Compos Struct 2013;106:549–59.
[12] Rivallant S, Bouvet C, Hongkarnjanakul N. Failure analysis of CFRP laminates subjected to compression after impact: FE simulation using discrete interface elements. Composites A 2013;55:83–93.
[13] Lin S, Thorsson SI, Waas AM. Predicting the low velocity impact damage of a quasi-isotropic laminate using EST. Compos Struct 2020;251:112530.
[14] Lin S, Waas AM. The effect of stacking sequence on the LVI damage of laminated composites; experiments and analysis. Composites A 2021;145:106377.
[15] Ebina M, Yoshimura A, Sakaue K, Waas AM. High fidelity simulation of low velocity impact behavior of CFRP laminate. Composites A 2018;113:166–79.
[16] Feng D, Aymerich F. Finite element modelling of damage induced by low-velocity impact on composite laminates. Compos Struct 2014;108:161–71.
[17] Zhang J, Zhang X. Simulating low-velocity impact induced delamination in composites by a quasi-static load model with surface-based cohesive contact. Compos Struct 2015;125:51–7.
[18] Zhang J, Zhang X. An efficient approach for predicting low-velocity impact force and damage in composite laminates. Compos Struct 2015;130:85–94.
[19] Liu P, Liao B, Jia L, Peng X. Finite element analysis of dynamic progressive failure of carbon fiber composite laminates under low velocity impact. Compos Struct 2016;149:408–22.
[20] Giannaros E, Kotzakolios A, Sotiriadis G, Kostopoulos V. A multi-stage material model calibration procedure for enhancing numerical solution fidelity in the case of impact loading of composites. J Composite Mater 2021;55(1):39–56.
[21] Caputo F, De Luca A, Lamanna G, Borrelli R, Mercurio U. Numerical study for the structural analysis of composite laminates subjected to low velocity impact. Composites B 2014;67:296–302.
[22] Sun X, Wisnom M, Hallett S. Interaction of inter- and intralaminar damage in scaled quasi-static indentation tests: Part 2 – numerical simulation. Compos Struct 2016;136:727–42.
[23] Sun X, Hallett S. Barely visible impact damage in scaled composite laminates: Experiments and numerical simulations. Int J Impact Eng 2017;109:178–95.
[24] Achard V, Bouvet C, Castanié B, Chirol C. Discrete ply modelling of open hole tensile tests. Compos Struct 2014;113:369–81.
[25] Lopes CS, Sádaba S, González C, Llorca J, Camanho PP. Physically-sound simulation of low-velocity impact on fibre reinforced laminates. Int J Impact Eng 2016;92:3–17.
[26] Trellu A, Bouvet C, Rivallant S, Ratsifandrihana L. A new interface element connecting 3D finite elements with non-coincident nodes to simulate delamination in composite laminates. Compos Struct 2020;252:112694.
[27] Falcó O, Ávila R, Tijs B, Lopes C. Modelling and simulation methodology for unidirectional composite laminates in a virtual test lab framework. Compos Struct 2018;190:137–59.
[28] Lopes CS, Gómez DG, Falcó O, Tijs BH. 19 - Stochastic virtual testing laboratory for unidirectional composite coupons: from conventional to dispersed-ply laminates. In: Van Paepegem W, editor. Multi-scale continuum mechanics modelling of fibre-reinforced polymer composites. Woodhead publishing series in composites science and engineering, Woodhead Publishing; 2021, p. 579–607.
[29] Baluch AH, Falcó O, Jiménez JL, Tijs BH, Lopes CS. An efficient numerical approach to the prediction of laminate tolerance to barely visible impact damage. Compos Struct 2019;225:111017.
[30] Tijs B, Doldersum M, Turon A, Waleson J, Bisagni C. Experimental and numerical evaluation of conduction welded thermoplastic composite joints. Compos Struct 2022;281:114964.
[31] Sun W, Guan Z, Li Z. Simulation of low velocity impact induced inter- and intra-laminar damage of composite beams based on XFEM. Appl Compos Mater 2017;24(6):1459–77.
[32] Bui TQ, Hu X. A review of phase-field models, fundamentals and their applications to composite laminates. Eng Fract Mech 2021;248:107705.
[33] ABAQUS version 6.14 online documentation, Analysis user's manual. SIMULIA Inc., Dassault Systèmes; 2013.
[34] Maimí P, Camanho PP, Mayugo JA, Dávila CG. A continuum damage model for composite laminates: Part I - Constitutive model. Mech Mater 2007;39:897–908.
[35] Catalanotti G, Camanho PP, Marques AT. Three-dimensional failure criteria for fiber-reinforced laminates. Compos Struct 2013;95:63–79.
[36] Bažant Z, Oh B. Crack band theory for fracture of concrete. Mater Struct 1983;16:155–77.
[37] AITM 1-0010. Determination of compression strength after impact. Technical Report, Blagnac Cedex, France: (Airbus Industrie Test Method); 2005.
[38] ASTM. Standard test method for measuring the damage resistance of a fiber-reinforced polymer matrix composite to a drop-weight impact event. Technical Report, West Conshohocken, PA, USA: American Society for Testing and Materials (ASTM); 2012, ASTM D 7136/D 7136M-12.
[39] BSS-7260. Boeing specification support standard. determination of compression strength after impact. Technical Report, Seattle, Washington: The Boeing Company; 1988.
[40] Petit S, Bouvet C, Bergerot A, Barrau J-J. Impact and compression after impact experimental study of a composite laminate with a cork thermal shield. Composites Sci Technol 2007;67(15):3286–99.
[41] Olsson R. Analytical prediction of large mass impact damage in composite laminates. Composites A 2001;32(9):1207–15.
[42] González E, Camanho PMP, Lopes C, Blanco N. Effects of ply clustering in laminated composite plates under low-velocity impact loading. Composites Sci Technol 2011;71(6):805–17.
[43] Camanho PP, Dávila CG, de Moura MF. Numerical simulation of mixed-mode progressive delamination in composite materials. Composite Mater 2003;37:1415–38.
[44] Turon A, Camanho PP, Costa J, Dávila C. A damage model for the simulation of delamination in advanced composites under variable-mode loading. Mech Mater 2006;38(11):1072–89.
[45] ASTM. Standard test method for short-beam strength of polymer matrix composite materials and their laminates. Technical Report, West Conshohocken, PA, USA: American Society for Testing and Materials (ASTM); 2000, ASTM D 2344-2344M(2000).
[46] Maimí P, Camanho PP, Mayugo JA, Dávila CG. A continuum damage model for composite laminates: Part II - computational implementation and validation. Mech Mater 2007;39:909–19.
[47] Ramberg W, Osgood WR. Description of stress–strain curves by three parameters. Natl Advis Comm Aeronaut 1943. Technical Note No. 902.
[48] Maimí P, Camanho PP, Mayugo JA, Dávila CG. A continuum damage model for composite laminates - part II: Computational implementation and validation. Mech Mater 2007;39:909–19.
[49] Maimí P. Modelización constitutiva y computacional del daño y la fractura de materiales compuestos [Ph.D. thesis], Universitat de Girona; 2006.
[50] Millen S, Ullah Z, Falzon B. On the importance of finite element mesh alignment along the fibre direction for modelling damage in fibre-reinforced polymer composite laminates. Compos Struct 2021;114694.
[51] Rajaneesh A, Ponthot J, Bruyneel M. High velocity impact response of composite laminates using modified meso-scale damage models. Int J Impact Eng 2021;147:103701.
[52] Garijo D, Martínez F, Lopes CS, Llorca J, González C, Puente JL, Loya JA, et al. 8.12 Multiscale FE modelling and design of composite laminates under impact. In: Beaumont PW, Zweben CH, editors. Comprehensive composite materials II. Oxford: Elsevier; 2018, p. 219–38.

[53] Puso MA. A highly efficient enhanced assumed strain physically stabilized hexahedral element. Int J Numer Methods Eng 2000;49(8):1029–64.
[54] DOT/FAA/AR-02/109. Guidelines and recommended criteria for the development of a material specification for carbon fiber/epoxy unidirectional prepregs. Technical Report, National Technical Information Service (NTIS), Office of Aviation Research; 2003, D. C. 20591.
[55] NCAMP. Hexcel 8552 AS4 unidirectional prepeg qualification statical analysis report. Technical Report, National Center for Advanced Materials Performance; 2011, CAM-RP-2010-002 May 6, Revision A.
[56] Koerber H, Xavier J, Camanho P. High strain rate characterisation of unidirectional carbon-epoxy IM7-8552 in transverse compression and in-plane shear using digital image correlation. Mech Mater 2010;42(11):1004–19.
[57] Cantwell W, Blyton M. Influence of loading rate on the interlaminar fracture properties of high performance composites-a review. 1999.
[58] May M. Measuring the rate-dependent mode I fracture toughness of composites – A review. Composites A 2016;81:1–12.
[59] Wang K, Zhao L, Hong H, Zhang J. A strain-rate-dependent damage model for evaluating the low velocity impact induced damage of composite laminates. Compos Struct 2018;201:995–1003.